applied sciences

MDPI

Article

Spherical Atomic Norm-Inspired Approach for Direction-of-Arrival Estimation of EM Waves Impinging on Spherical Antenna Array with Undefined Mutual Coupling

Oluwole John Famoriji * and **Thokozani Shongwe**

Department of Electrical and Electronic Engineering Science, University of Johannesburg, Auckland Park, 2006, Johannesburg P.O. Box 524, South Africa
* Correspondence: famoriji@mail.ustc.edu.cn

Abstract: A spherical antenna array (SAA) is an array-designed arrangement capable of scanning in almost all the radiation sphere with constant directivity. It finds recent applications in aerospace, spacecraft, vehicular and satellite communications. Therefore, estimation of the direction-of-arrival (DoA) of electromagnetic (EM) waves that impinge on an SAA with unknown mutual coupling called for research attention. This paper proposed a spherical harmonic atomic norm minimization (SHANM) for DoA estimation using an SAA configuration. The gridless sparse signal recovery problem is considered in the spherical harmonic (SH) domain in conjunction with the atomic norm minimization (ANM). Because of the unavailability of the Vandermonde structure in the SH domain, the theorem of Vandermonde decomposition that is the mathematical basis of the traditional ANM methods finds no application in SH. Addressing this challenge, a low-dimensional semidefinite programming (SDP) approach implementing the SHANM method is developed. This approach is independent of Vandermonde decomposition, and directly recovers the atomic decomposition in SH. The numerical experimental results show the superior performance of the proposed method against the previous methods. In addition, accounting for the impacts of mutual coupling, an experimental measured data, which is the generally accepted ground of testing any method, is employed to illustrate the efficacy and robustness of the proposed methods. Finally, for achieving DoA estimation with sufficient localization accuracy using a SAA, the proposed SHANM-based method is a better option.

Keywords: atomic norm; SH; SDP; DoA estimation; SAA; gridless sparse signal recovery

check for updates

Citation: Famoriji, O.J.; Shongwe, T. Spherical Atomic Norm-Inspired Approach for Direction-of-Arrival Estimation of EM Waves Impinging on Spherical Antenna Array with Undefined Mutual Coupling. *Appl. Sci.* **2023**, *13*, 3067. https://doi.org/10.3390/app13053067

Academic Editor: Daniele Funaro

Received: 1 February 2023
Revised: 20 February 2023
Accepted: 22 February 2023
Published: 27 February 2023

1. Introduction

Various uses of antenna array signal processing depend on the direction-of-arrival (DoA) estimation, which includes separation of source, spatial filtering, etc. For instance, DoA estimation of a signal source is specifically important in robotics where the direction tracking of one or more moving sources permits the recognition of the local surroundings, which is required in adequate human to robot communication [1–4]. Generally speaking, the existing methods can be roughly classified into the super-resolution-based methods and Fourier-transformation-based methods. The angular resolution of the Fourier-based methods is force-limited by the Rayleigh criterion, and those methods with better resolution performance than the Rayleigh criterion are referred to as super-resolution methods. Source signal localization also finds application in signal improvement, signal detection, automated steering of cameras, and source tracking, among others. DoA information ensures adaptive beamforming of the received mode pattern for an improved sensitivity of the system in the desired wave directions, and reduces unwanted interferences [5]. Simply put, it makes the antenna generate a maximal beam in the users' desired direction and nulls in the interference direction, consequently enhancing the behavior of base and mobile stations.

Hence, estimation of the DoA of electromagnetic waves (EM) impinging on antenna arrays remains an important and crucial task.

The spherical antenna array (SAA) (depicted in Figure 1) satisfies isotropic requirements [6]. The SAA configuration exhibits the capability to receive signals in all directions with the same strength regardless of the DoA and the polarization [2,5]. In order to explore the biggest degree of freedom, the SAA must have the ability to determine the polarization and DoA of the receiving signals impinging on the unit sphere. There are various postulates that describe the SAA in literature [1,3,5,7–15], but correct theories with deeper intuition of the signal features of the SAA still beg for research curiosity and attention.

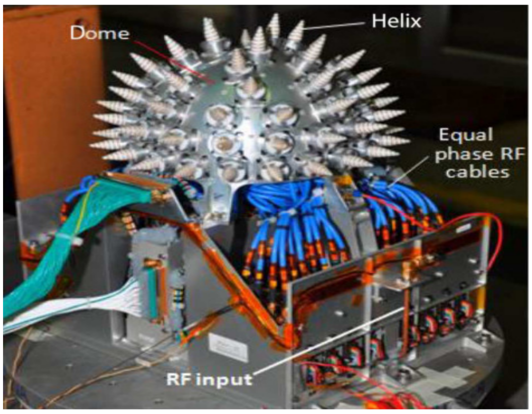

Figure 1. A connected 64-element SAA in anechoic chamber [8].

Various methods or algorithms have been developed for DoA estimation in the spherical harmonic (SH) domain [16–22]. A good number of these methods calculate metrics over a dense azimuth–elevation grid in advance of the identification of peaks as the DoAs. Such algorithms are those that deal with the computation of the steered response power, because of beamformers that steer in all the source directions, and those that calculate the spatial spectrum via subspace techniques based on MUSIC (multiple signal classification) [5]. There are widely used methods, such as, the MUSIC method [1], ESPRIT (estimation of signal parameters through rotational invariance technique) method [5], beamforming, and ML (maximum likelihood) approaches [4,15]. The above techniques have been investigated and employed for antenna arrays having arbitrary configurations and produce correct estimation of DoA. There are more approaches, such as MUSIC group delay [4], the SRP-PHAT (steered response power with phase transform) approach [5], GCC (generalized cross-correlation) technique [1,5] adaptive eigenvalue decomposition method [13], 1-D MUSIC [11] method, and order aware algorithm [8]. In near field, the MUSIC method employed for spherical configurations [1–3,5] is called SH-MUSIC. Because of the sensitivity of SH-MUSIC to distortions in the multipath case, Nakamura in [13] developed another approach named direct path dominance (DPD). In the near field, the mode strength depends on a source range that is not known a priori. Hence, DPD is measured in the dimension of time; as such, SH-DPD-MUSIC utilizes higher frames [1]. If near-field frequency smoothing is applied, then a range dependent source normalization is a requirement. Therefore, other DoA estimation methods are broken down into the SH domain, which is the minimum variance distortionless response (MVDR) [8].

At present, different methods for DoA estimation employ a spatial covariance matrix [5,11,18,19,22–24]. For instance, the steer response power map generated by MVDR (minimum variance distortionless response) beamformer rejects background noise optimally for all look directions through the adjustment of the beam pattern based on the MUSIC and spatial covariance matrix [25], which decomposes the spatial covariance matrix into noise and signal subspaces. The MVDR beamformer comes up as the error in the placement of beam pattern loss. MUSIC, based on the linear dependency of the reflections on the direct path signals, implies the covariance matrix rank is made smaller and the division between the noise and signal subspaces may be prone to errors.

The generally established mutual coupling correction approaches for antenna arrays are classified into two classes. The first class deals with the compensation of or calibration of mutual coupling in decoupled network design and antenna array design. In the second class, the mutual coupling is corrected by solving the mutual coupling matrix (MCM) via array signal processing and analysis of electromagnetics (EM) [25]. The implementation of the first approach is more challenging in engineering. The approach is based on the analysis of EM, such as the S-scattering parameter technique, and open-circuit voltage techniques are only applied to transmit mode arrays. The full-wave approach and reception of the mutual impedance approach require larger measurement data, and the steps involved are complicated. From the perspective of array signal processing, the blind calibration approach uses an MCM banded symmetric Toeplitz structure. Mutual coupling calibration can be achieved using matrix transformation or separation of the mutual coupling coefficient. The blind calibration approach, when combined with the estimation algorithm, simultaneously estimates mutual coupling parameters and DoAs [26].

Motivated by the sparse representation method [26,27], spherical sparse signal processing has drawn attention recently. For instance, [28,29], studied sparse recovery for random sampling in the SH domain. In [30,31], sparse Bayesian learning techniques for DoA estimations were developed in the SH domain. This sparse Bayesian learning technique could exhibit better performance than the ℓ_1 norm dependent ones [27], and they have slow rates of convergence. In addition, grid mismatch issues degrade the aforementioned sparsity-dependent methods. Dealing with this issue, research has been conducted to remove the grid modeling error [32].

Lately, a unified scheme was developed for the representation of sparse signals on the infinite or finite dimensional dictionary in [33]. It leads to the gridless sparse recovery technique by resolving the optimization problem on the convex hull of an atomic set that is recognized as atomic norm minimization (ANM). Particularly, atoms that are described by complex exponentials, Candes and Fernandez-Granda depict that bandlimited signals are recoverable provided the low-rate samples frequency separation condition is ensured [34]. According to theory, the ANM method is extended to multidimensional frequency models [35–37], prior knowledge [38], multi-measurement vectors [39] and covariance matrix scenarios [40–42] for DoA estimation and gridless signal recovery. Conversely, the traditional ANM techniques are based on the array manifold's Vandermonde structure, and therefore applicable only to linear/rectangular arrays.

Using the spherical ANM method in [43] is an easy way to solve the traditional ANM problem where the elements of the atom are Vandermonde vectors with extra weighting constrains [44–47]. This method leads to a potential larger dimensional semidefinite programming (SDP) challenge than the dimension of samples, that could be computationally challenging. Based on the detailed real-time utilizations for gridless sparse depiction techniques on the SH manifolds of the DoA, we are inspired to propose a low-dimensional SH ANM method, which is not yet available in the literature. Moreover, it becomes important to state that Jie Pan [48] first proposed SHANM. The main novelty of this research in comparison to [48] is that we specifically extended the SHANM technique to an antenna array as opposed to a microphone array, supported with real antenna measurement data in electromagnetics vis-à-vis an SAA, which is the most acceptable justification to examine and test each method. The main contributions of this paper are summarized as follows.

(a) The gridless sparse signal recovery problem of SH manifolds is studied using ANM for DoA estimation of signal impinging on an SAA.
(b) The SH atomic norm based on a covariance matrix is defined. Because the SH is not Vandermonde, the main problem in the extension of the ANM method to the SH is the formulation of the convex optimization problem without the Vandermonde decomposition theorem. Dealing with this problem, a low-dimensional semidefinite programming formulation of the SHANM problem is developed, which consequently

recovers the atomic decomposition directly with no foundation of the Vandermonde decomposition theorem.

(c) Consequently, an SHANM-based DoA estimation method is presented for SAA configurations and exhibits improved performance compared to previous methods, particularly at low SNR (signal-to-noise ratio) and in the case of adjacent sources.

(d) In addition, with the current development in technologies and applications, systems and circuits are becoming more compact every day, causing the distance between the elements in the array to be smaller, consequently causing strongly coupled antenna arrays. This primarily lead to strong mutual coupling, impedance mismatch, and poor radiation features [49]. Hence, estimating the DoA with mutual coupling remains an important task. In this work, we accounted for the impacts of mutual coupling using experimental measured data [8], which is the general and acceptable ground to examine any method, which we employed to illustrate the efficacy and robustness of the proposed methods. The proposed method shows sufficient localization accuracy.

2. Signal Model

Considering a spherical antenna array V, the vth radiator is located at $\boldsymbol{u}_v = (R, \phi_v)$, where $\phi_v = (\theta_v, \varphi_v)$. R, θ, φ represent the radius, elevation, and azimuth. There exist I far field sources situated at $\psi_i = (\theta_v, \varphi_v) \in \xi$ with $\xi = \{(\theta, \varphi)|\theta \in (0, \pi], \varphi \in (-\pi, \pi]\}$. The signal impinging on the SAA $\boldsymbol{G}(t)$ is

$$\boldsymbol{G}(t) = \boldsymbol{A}(\overrightarrow{\psi})\boldsymbol{s}(t) + \boldsymbol{n}(t) \tag{1}$$

where $\boldsymbol{s}(t)$ and $\boldsymbol{n}(t)$ denote the source and noise, respectively. $\boldsymbol{A}(\overrightarrow{\psi})$ is the array manifold, $\boldsymbol{A}(\overrightarrow{\psi}) = [\boldsymbol{a}(\psi_i), \ldots, \boldsymbol{a}(\psi_I)] \in \mathbb{C}^{V \times I}$.

If $Y_n^m(\theta, \varphi)$ represents the SH of order n and degree m, then

$$\begin{gathered} Y_n^m(\theta, \varphi) = \sqrt{\frac{(2n+1)(n-m)!}{4\pi(n+m)!}} P_n^m(cos\theta) e^{im\varphi} \\ \forall 0 \leq n \leq N,\ 0 \leq m \leq n \end{gathered} \tag{2}$$

$P_n^m(cos\theta)$ denotes the connected Legendre polynomial, the vth element of $\boldsymbol{a}(\psi_i)$ is then formulated as the SH series decomposition by neglecting the high order $b_n(\kappa R)$ when $n > \kappa R$ [50]

$$a_v(\psi_i) = \sum_{n=0}^{N} \sum_{m=-n}^{n} b_n(\kappa R)[Y_n^m(\psi_i)]^* Y_n^m(\phi_i) \tag{3}$$

where N is the maximum SH order, $\kappa = \lambda/2\pi$ and λ denotes the wavelength, and the frequency dependent constituent $b_n(\kappa R)$ is expressed as [50]

$$b_n(\kappa R) = \begin{cases} 4\pi i^n J_n(\kappa R) \quad open\ sphere \\ 4\pi i^n (J_n(\kappa R) - \frac{J_n'(\kappa R)}{u_n'(\kappa R)} \quad u_n(\kappa R)) \quad rigid\ sphere \end{cases} \tag{4}$$

u_n and J_n are the second kind of spherical Hankel function and the first kind of spherical Bessel function, correspondingly. J_n' and u_n' are the derivatives of J_n and u_n, respectively.

So, in matrix form, the SAA model is

$$\boldsymbol{A}(\overrightarrow{\psi}) = \boldsymbol{Y}(\overrightarrow{\phi})\boldsymbol{B}\boldsymbol{Y}^H(\overrightarrow{\psi}) \tag{5}$$

where the vth original vector of $\boldsymbol{Y}(\overrightarrow{\phi}) \in \mathbb{C}^{V \times (N+1)^2}$ and the kth original vector of $\boldsymbol{Y}(\overrightarrow{\psi}) \in \mathbb{C}^{I \times (N+1)^2}$ are defined as [50].

$$\begin{aligned} \boldsymbol{y}(\phi_v) &= \left[Y_0^0(\phi_v), Y_1^{-1}(\phi_v), Y_1^0(\phi_v), \ldots, Y_N^N(\phi_v)\right], \\ \boldsymbol{y}(\psi_i) &= \left[Y_0^0(\psi_i), Y_1^{-1}(\psi_i), Y_1^0(\psi_i), \ldots, Y_N^N(\psi_i)\right] \end{aligned} \tag{6}$$

and $\boldsymbol{B} \in \mathbb{C}^{(N+1)^2 \times (N+1)^2}$ is

$$\boldsymbol{B} = diag(b_0(\kappa R), \ldots, b_N(\kappa R)). \tag{7}$$

Applying the SH transformation as

$$\boldsymbol{P}(t) = \boldsymbol{Y}^H(\vec{\phi})\mathcal{H}\boldsymbol{G}(t) = \boldsymbol{B}\boldsymbol{Y}^H(\vec{\psi})\boldsymbol{s}(t) + \boldsymbol{c}(t) \tag{8}$$

where $\mathcal{H} = diag(\alpha_1, \alpha_2, \ldots \alpha_v)$ satisfies [50,51]

$$\boldsymbol{Y}^H(\vec{\phi})\mathcal{H}\boldsymbol{Y}(\vec{\phi}) = \boldsymbol{I}. \tag{9}$$

$\boldsymbol{c}(t)$ represents the reshaped/transform added noise. Hence, the SH covariance matrix is expressed as

$$\boldsymbol{R} = E\left\{\boldsymbol{P}(t)\boldsymbol{P}^H(t)\right\} = \boldsymbol{B}\boldsymbol{Y}^H(\vec{\psi})\boldsymbol{R}_s\boldsymbol{Y}(\vec{\psi})\boldsymbol{B}^H + \boldsymbol{C} \tag{10}$$

with $\boldsymbol{C} = E\{\boldsymbol{c}(t)\boldsymbol{c}^H(t)\}$ and $\boldsymbol{R}_s = E\{\boldsymbol{s}(t)\boldsymbol{s}^H(t)\}$. We can remark that if $E\{\boldsymbol{n}(t)\boldsymbol{n}^H(t)\} = \sigma^2\boldsymbol{I}$, where σ^2 denotes the noise power. The position of the SAA elements $\vec{\phi}$ satisfies the spherical t-design configuration in [50] ($\mathcal{H} = \boldsymbol{I}$), then $\boldsymbol{C} = \sigma^2 I$.

Considering the v*th* column of $\mathbf{R}$ in Equation (10) to be $\boldsymbol{r}_v$ which can be regarded as one array measurement. Thus, if $\boldsymbol{H} = \boldsymbol{R}_s\boldsymbol{Y}(\vec{\psi})\boldsymbol{B}^H$, $\boldsymbol{r}_v$ can be remodeled as

$$\boldsymbol{r}_v = E\{\boldsymbol{P}(t)\boldsymbol{P}_v{}^*(t)\} = \boldsymbol{B}\boldsymbol{Y}^H(\vec{\psi})\boldsymbol{h}_v + \boldsymbol{c}_v \tag{11}$$

where $\boldsymbol{P}_v(t)$ is the ith row of $\boldsymbol{P}(t)$, $\boldsymbol{h}_v$ and $\boldsymbol{c}_v$ are the vth column of $\mathbf{H}$ and $\mathbf{C}$, respectively. From Equations (10) and (11), the SH covariance matrix in matrix form is [52]

$$\boldsymbol{R} = \boldsymbol{B}\boldsymbol{Y}^H(\vec{\psi})\boldsymbol{H} + \boldsymbol{C} = \sum_{q=1}^{Q} u_q\boldsymbol{B}\boldsymbol{Y}^H(\vec{\psi})\boldsymbol{\rho}_q + \boldsymbol{C} \tag{12}$$

where u_q represents the Euclidean norm of kth raw of $\boldsymbol{H}$ and $\boldsymbol{\rho}_q$ is the normalized kth raw vector of $\boldsymbol{H}$, i.e., $\|\boldsymbol{\rho}_q\|_2 = 1$.

It can be noted that the covariance matrix $\boldsymbol{R}$ in Equation (12) shows a multiple measurement vector formulation, through which a different atomic norm compact derivation can be developed for the covariance matrix as below.

3. Atomic Norm in the Spherical Domain

From the framework developed in [53], an atomic set where the elements are the groundwork of depiction to the signals is evaluated. For SH signals, the atomic set Γ is a function of the atoms in SH vectors $\boldsymbol{Y}(\psi)$ and the signals is expressed as a sum of different atoms

$$\boldsymbol{g} = \sum_{q=1}^{Q} u_q\boldsymbol{Y}(\psi_q), \qquad \boldsymbol{Y}(\psi_q) \in \boldsymbol{\Gamma}. \tag{13}$$

Equation (13) is known and considered to be atomic decomposition. Evaluating the most sparse atomic decomposition of $\boldsymbol{g}$ will always give the l_0 SH atomic norm as

$$\|\boldsymbol{g}\|_{\boldsymbol{\Gamma},\boldsymbol{0}} = inf\left\{K \middle| \boldsymbol{g} = \textstyle\sum_{q=1}^{Q} u\psi_q\boldsymbol{Y}(\psi_q), \boldsymbol{Y}(\psi_q) \in \boldsymbol{\Gamma}\right\}. \tag{14}$$

Recovering the wave within a convex optimization framework, reference [53] opined a convex heuristic of the l_0 atomic norm, expressed as

$$\|\boldsymbol{g}\|_{\boldsymbol{\Gamma}} = \inf\{t > 0 : x \in t\, conv(\Gamma)\}, \tag{15}$$

where $conv(\Gamma)$ is the convex hull of Γ. Therefore,

$$\|\boldsymbol{g}\|_{\boldsymbol{\Gamma}} = \inf\left\{\sum_{q=1}^{Q} u\psi_q | \boldsymbol{g} = \sum_{q=1}^{Q} u\psi_q \boldsymbol{Y}(\psi_q), \boldsymbol{Y}(\psi_q) \in \boldsymbol{\Gamma}\right\}, \tag{16}$$

which is called the SH atomic norm, and the respective dual norm $\|\cdot\|_{\boldsymbol{\Gamma}}^{*}$ becomes [54]

$$\|\boldsymbol{g}\|_{\boldsymbol{\Gamma}}^{*} = \sup_{\|\boldsymbol{g}\|_{\boldsymbol{\Gamma}} \leq 1} R_e\left\{Tr\left[\boldsymbol{g}^H \partial\right]\right\}, \tag{17}$$

For the covariance matrix, different atomic norms type are already proposed [55–57]. This article develops another atomic norm of the covariance matrix for DoA estimation using SAA.

Observing the multiple measurement vector model, an ideal (no noise) covariance matrix in Equation (12), $\boldsymbol{R} = \sum_{\boldsymbol{q}=\boldsymbol{1}}^{\boldsymbol{Q}} u_q \boldsymbol{B}\boldsymbol{Y}^H(\psi_q)\boldsymbol{\rho}_q$, then the SH atomic set is defined as

$$\Gamma := \left\{\mathbf{B}, \boldsymbol{Y}^H(\psi_q)\rho \middle| \psi \in, \ \|\boldsymbol{\rho}\|_2 = 1\right\}. \tag{18}$$

Furthermore, the spherical harmonic l_0 norm of the covariance matrix $\boldsymbol{R}$ can be described as

$$\|\boldsymbol{R}\|_{\Gamma,0} = \inf\left\{I | \boldsymbol{R} = \sum_{\boldsymbol{q}=\boldsymbol{1}}^{\boldsymbol{Q}} u_{\boldsymbol{q}} \boldsymbol{B}\boldsymbol{Y}^H(\boldsymbol{\psi_q})\boldsymbol{\rho_q}.v_q \geq 0\right\}, \tag{19}$$

the SH atomic norm of $\boldsymbol{R}$ is expressed as

$$\|\boldsymbol{R}\|_{\Gamma} = \inf\left\{\sum_{q=1}^{Q} u_{\boldsymbol{q}} | \boldsymbol{R} = \sum_{\boldsymbol{q}=\boldsymbol{1}}^{\boldsymbol{Q}} u_{\boldsymbol{q}} \boldsymbol{B}\boldsymbol{Y}^H(\psi_q)\boldsymbol{\rho_q}.v_q \geq 0\right\}, \tag{20}$$

The section may be divided by subheadings. It should provide a concise and precise description of the experimental results, their interpretation, as well as the experimental conclusions that can be drawn.

4. Resolving the SHANM with SDP

The traditional ANM approaches for the linear spectrum is a function of the theorem of Vandermonde decomposition to generate the SDP corresponding execution. However, this method is not directly extendable to SHANM in Equation (20), because of the basic problem that SH vectors do not have a Vandermonde structure. Dealing with this problem in this section, we propose an SDP for the SHANM challenge.

4.1. SDP of SHANM

It can be noted that $P_n^m(cos\theta)$ is an order n trigonometric polynomial, $P_n^m(cos\theta) = \sum_{v=-n}^{n} \gamma_{n,m,l} e^{iv\theta}$ with unique coefficients $\{\gamma_{n,m,l}\}$, and the SH in Equation (2) is described using Fourier series as [58]

$$Y_n^m(\theta, \varphi) = \sum_{l=-n}^{n} A_{n,m}\gamma_{n,m,l} e^{il\theta} e^{im\varphi}, \tag{21}$$

where $A_{n,m} = \sqrt{\frac{(2n+1)(n-m)!}{4\pi(n+m)!}}$. From Equation (21), Equation (8) can be rewritten as

$$\boldsymbol{P}(t) = \boldsymbol{BOD}(\overrightarrow{\psi})\boldsymbol{s}(t) + \boldsymbol{c}(t) \tag{22}$$

where $\boldsymbol{D}(\overrightarrow{\psi}) = [\boldsymbol{f}(\psi_1), \ldots, \boldsymbol{f}(\psi_I)$, and $\boldsymbol{f}(\psi_I) = \boldsymbol{f}_\theta(\theta_i) \otimes \boldsymbol{f}_\varphi(\varphi_i)$, $\boldsymbol{f}_\theta(\theta_i) = \left[e^{-iN\theta_i}, \ldots, 1, \ldots, e^{iN\theta_i}\right]^T$,

$$\boldsymbol{f}_\varphi(\varphi_i) = \left[e^{-iN\varphi_i}, \ldots, 1, \ldots, e^{iN\varphi_i}\right]^T, \tag{23}$$

O denotes a constant matrix generated by $A_{n,m}\gamma_{n,m,l}$. Hence, putting Equation (22) into Equation (12), we have

$$\boldsymbol{R} = E\left\{\boldsymbol{P}(t)\boldsymbol{P}^H(t)\right\} = \widetilde{\boldsymbol{O}}\boldsymbol{D}(\overrightarrow{\boldsymbol{\psi}})\boldsymbol{R_s}\boldsymbol{D}^H(\overrightarrow{\psi})\widetilde{\boldsymbol{O}}^H + \boldsymbol{C} \tag{24}$$

where $\widetilde{\boldsymbol{O}} = \boldsymbol{BO}$.

Using the relationship shown in Equation (24) regarding the spherical harmonic steering vector and Vandermonde matrix, starting with a noiseless scenario where $C = 0$ we arrive at the low-dimensional SDP implementation for the SHANM method.

Proposition 1. *For certain location sources $\overrightarrow{\psi}$, assuming the objective value of the subsequent optimization puzzle gives the norm $\|\boldsymbol{R}\|_T$, implying*

$$\begin{aligned} \|\boldsymbol{R}\|_T = \min_{\boldsymbol{Q},\boldsymbol{M}} \tfrac{1}{2\varkappa^2} Tr(\widetilde{\boldsymbol{O}}S(\boldsymbol{Z})\widetilde{\boldsymbol{O}}^H) + \tfrac{1}{2}Tr(\boldsymbol{M}) \\ s.t. \begin{bmatrix} \widetilde{\boldsymbol{O}}S(\boldsymbol{Z})\widetilde{\boldsymbol{O}}^H & \boldsymbol{R} \\ \boldsymbol{R}^H & \boldsymbol{M} \end{bmatrix} \geq 0, \end{aligned} \tag{25}$$

if the highest SH order N is high enough and a strong duality condition is ensured, then $\|\boldsymbol{R}\|_T = \|\boldsymbol{R}\|_\Gamma$, where $\|\boldsymbol{R}\|_\Gamma$ is the SH atomic norm described in Equation (20) with $\boldsymbol{R} \in \mathbb{C}^{(N+1)^2 \times (N+1)^2}$.

$$\varkappa = \|\widetilde{\boldsymbol{O}}\|_F = \sqrt{\sum_{l=0}^{N} \frac{(4\boldsymbol{l}+1)}{4\pi}}\|\boldsymbol{B}\|_F, \tag{26}$$

and $S(\boldsymbol{Z})$ is a Hermitian matrix, which is a function of $\boldsymbol{Z}$ as [35]

$$S(\boldsymbol{Z}) = \begin{bmatrix} \boldsymbol{Z}_0 & \boldsymbol{Z}_{-1} & 0 & \boldsymbol{Z}_{-2N} \\ \boldsymbol{Z}_1 & \boldsymbol{Z}_0 & 0 & \boldsymbol{Z}_{-2N+1} \\ \vdots & \vdots & \ddots & \vdots \\ \boldsymbol{Z}_{2N} & \boldsymbol{Z}_{2N-1} & \cdots & \boldsymbol{Z}_0 \end{bmatrix} \tag{27}$$

where $\boldsymbol{Z}_v$ is a Toeplitz matrix described by lth row of $\boldsymbol{Z}$ to be

$$\boldsymbol{Z}_l = \begin{bmatrix} \boldsymbol{Z}_{l,0} & \boldsymbol{Z}_{l,-1} & \cdots & \boldsymbol{Z}_{l,-2N} \\ \boldsymbol{Z}_{l,1} & \boldsymbol{Z}_{l,0} & \cdots & \boldsymbol{Z}_{l,-(2N-1)} \\ \vdots & \vdots & \ddots & \vdots \\ \boldsymbol{Z}_{l,2N} & \boldsymbol{Z}_{l,2N-1} & \cdots & \boldsymbol{Z}_{l,0} \end{bmatrix} \tag{28}$$

4.2. Signal Denoising of SHANM

This subsection deals with noisy scenarios when $\boldsymbol{C} \neq 0$. The estimation of the covariance matrix obtained through averaging the snapshots in a practical sense is

$$\hat{\boldsymbol{R}} = \frac{1}{J}\sum_{t=1}^{J} \boldsymbol{P}(t)\boldsymbol{P}^H(t) = \widetilde{\boldsymbol{O}}\boldsymbol{D}(\overrightarrow{\boldsymbol{\psi}})\boldsymbol{R_s}\boldsymbol{D^H}(\overrightarrow{\psi})\widetilde{\boldsymbol{O}}^H + \varsigma = \overline{\boldsymbol{R}} + \varsigma \tag{29}$$

where ς denotes the outlier from the added noise and the impact of finite snapshots. A normal method of dealing with the additional noise for the sparse problem is regularization.

According to [58], for recognized sources, the least fitting error ε could come out to be the best option, where there is unnoticeable false alarm. Therefore, the signal denoising problem by SHANM is expressed as

$$\min_{\boldsymbol{Z},\boldsymbol{M},\boldsymbol{R}} \frac{1}{2\varkappa^2} Tr\left(\widetilde{\boldsymbol{O}}S(\boldsymbol{Z})\widetilde{\boldsymbol{O}}^H\right) + \frac{1}{2}Tr(\boldsymbol{M}) \; s.t. \begin{bmatrix} \widetilde{\boldsymbol{O}}S(\boldsymbol{Z})\widetilde{\boldsymbol{O}}^H & \boldsymbol{R} \\ \boldsymbol{R}^H & \boldsymbol{M} \end{bmatrix} \geq 0 \quad \|\hat{\boldsymbol{R}} - \boldsymbol{R}\|_2^2 \leq \varepsilon^2 \tag{30}$$

where $\varepsilon = \|\varsigma\|_2$ is the optimal choice for covariance matrix $\mathbf{R}$ recovery. However, it is shown here that $\varepsilon = (N+1)^2\sigma^2$.

5. Direction-of-Arrival Estimation

In the previous section, a low-dimensional SDP that is a function of the SH atomic norm minimization (SHANM) method for gridlesss sparse signal recovery on the manifolds in the SH domain is presented, which produced source localization. Here, it is demonstrated how the developed algorithm estimate the DoA using an SAA in free space.

Assuming a far field, the point source estimate of the DoA using an SAA is defined as recognizing atoms from measurements in the SH domain, and therefore executable based on the SHANM method.

The DoA estimation using the SHANM-based approach steps from the recovered covariance matrix

$$\widetilde{\boldsymbol{R}^\star} = \widetilde{\boldsymbol{O}}S\left(\widetilde{\boldsymbol{Z}^\star}\right)\widetilde{\boldsymbol{O}}^H, \tag{31}$$

where $\widetilde{\boldsymbol{Z}^\star}$ represents the optimal solution of Equation (30). Extracting the DoAs using the SHANM-based method in Equation (31), the following analysis is given.

Based on Proposition 1, $(\boldsymbol{Z}^\star, \boldsymbol{M}^\star)$ expressed as

$$\begin{aligned} S(\boldsymbol{Z}^\star) &= \sum_{i=1}^{I} q_i \boldsymbol{f}(\psi_i)\boldsymbol{f}^H(\psi_i), \\ \boldsymbol{M}^\star &= \sum_{i=1}^{I} q_i \boldsymbol{\rho}_i \boldsymbol{\rho}_i^H, \end{aligned} \tag{32}$$

Therefore, it can be said that the principal component of $\widetilde{\boldsymbol{R}^\star}$ spans the space range of Equation (32). This inspired the application of the subspace approach to the recovered covariance matrix $\widetilde{\boldsymbol{R}^\star}$ to be

$$\widetilde{\boldsymbol{R}^\star} = \boldsymbol{U}_s \sum_s \boldsymbol{U}^H{}_s + \sigma^2 \boldsymbol{U}_N \boldsymbol{U}_N^H. \tag{33}$$

Decomposition of the eigenvalue of $\widetilde{\boldsymbol{R}^\star}$ produces the signal subspace $\boldsymbol{U}_s$ and noise subspace $\boldsymbol{U}_N$, and then

$$\Xi(\boldsymbol{U}_s) \approx \Xi(\boldsymbol{B}\boldsymbol{Y}^H(\vec{\psi})) \tag{34}$$

where $\Xi(\cdot)$ represents the spanned subspace, such that the SH-ESPRIT algorithm is applicable to $\boldsymbol{U}_s$ for 2D estimation of DoA. Furthermore, the Legendre polynomial recurrence relationship, assuming

$$\begin{aligned} \boldsymbol{D}_1 &= diag\{\ 0\ , -1,\ 0,\ 1, \ldots, -N+1, \ldots, N-1\}, \\ \boldsymbol{D}_2 &= diag\left\{ I^-_{1,0},\ I^-_{2,-1}, I^-_{2,0}, I^-_{2,1}, \ldots, I^-_{N,-N+1}, \ldots, I^-_{N,N-1} \right\}, \\ \boldsymbol{D}_3 &= diag\left\{ I^+_{1,0},\ I^+_{2,-1}, I^+_{2,0}, I^+_{2,1}, \ldots, I^+_{N,-N+1}, \ldots, I^+_{N,N-1} \right\} \end{aligned} \tag{35}$$

and

$$\boldsymbol{E} = \boldsymbol{D}_2 \boldsymbol{U}_s^{(-1)} \boldsymbol{D}_3 \boldsymbol{U}_s^{(1)} \tag{36}$$

where $I^{\pm}_{n,m} = \sqrt{(n \mp m)(n \pm m + 1)}$ and $\boldsymbol{U}_s^{(-1)}$, $\boldsymbol{U}_s^{0}$, $\boldsymbol{U}_s^{(1)}$ is produced from $\boldsymbol{U}_s$ [55], then

$$\boldsymbol{D}_1 \boldsymbol{U}_s^0 = \boldsymbol{E}\begin{bmatrix} \bigcap^T \\ \bigcap^H \end{bmatrix}, \tag{37}$$

then $\bigcap$ can be expressed as

$$\bigcap = \left(\boldsymbol{E}^H \boldsymbol{E}\right)^{-\mathbf{1}} \boldsymbol{E}^H \boldsymbol{D}_1 \boldsymbol{U}_s^0. \tag{38}$$

The computation of eigenvalues u_i, $i = 1, 2, \ldots, I$, of $\bigcap$, the DoA of the *ith* source can be obtained by $\hat{\theta}_i = \tan^{-1}|u_i|$ and $\hat{\varphi}_i = \arg(u_i)$, respectively.

6. Numerical Simulation, and Experiment

Here, the proposed SHANM-based DoA estimation method is evaluated and analyzed against the l_1 norm dependent approach in [51], the SH-ESPRIT in [52], TSDA (elevation estimations with U-SH-ESPRIT and azimuths estimation with U-SH-RMUSIC) in [53], CV-VSBL in [54] and Cramer–Rao bound (CRB) in [55]. Comparisons were also made among the methods using real measurement data from the experiment, which in the end, is the acceptable ground to test any procedure.

Firstly, an SAA with radius, $r = 1.8$ cm, and made up of 32 radiators operating at 8.4 GHz (Figure 1) that are uniformly positioned on a rigid sphere, is utilized during numerical experiments or simulations [6,8,11]. The range between two consecutive samples in the uniform sampling framework remains constant. The uniform sampling framework gives rise to small platonic solids. The event appears majorly for a specific number of elements [6]. The highest order of the SAA is 4. A total of 600 different Monte Carlo simulations were conducted using Matlab software (2019b version) operating on a laptop personal computer (PC); Intel CPU, Core i7-8565U, 8th Gen., RAM 16 GB, 1 Terabyte. We employed two iterations in the simulations. To avoid aliasing problems, kr was maintained to be smaller than order N. In addition, narrowband amplitude modulation (AM) waves at far field were employed in each simulation case. Both the SHANM approach and SH-ESPRIT are referred to as SH-ANM-ESPRIT. The approaches that are based on discretion sparsity estimated DoAs via searching for the I biggest spectrum peaks using 0.2° grid interval. The performance metric used was the root mean square error (RMSE), and it is expressed as

$$RMSE = \sqrt{\frac{1}{MI}\sum_{i=1}^{I}\sum_{j=1}^{M}(\hat{\theta}_{ij} - \theta_i)} \tag{39}$$

where M is the number of simulation trials, and I is the number of source. $\hat{\theta}_{ij}$ and θ_i represent the estimates and the true value of the ith DoA at the jth attempt.

6.1. Resolution Ability Comparison

It is assumed that two sources are situated at $(\theta, \varphi) = (40^\circ, 60^\circ)$ and $(40^\circ + \vartheta, 60^\circ + \vartheta)$, and the angle of separation ϑ ranges from 1° to 30°. The on-sphere super resolution approach presented by Bendory et al. [58] as S-R-Sphere is referred to and compared with the average error of the DoA estimates of the SH-ANM-ESPRIT approach and S-R-Sphere approach under an ideal (without noise) single snapshot scenario. The average estimate error of 250 trials against the angle of separation is as depicted in Figure 2. It can be observed that both approaches share identical error levels in the estimation of the DoA, i.e., they probably share a similar resolution. Evaluating the complexity in computation, the average run time for each trial was computed for the two approaches. The proposed approach took about 0.5499 s and the S-R-Sphere approach took 1.3737 s per trial. This implies that the proposed method is more computationally efficient.

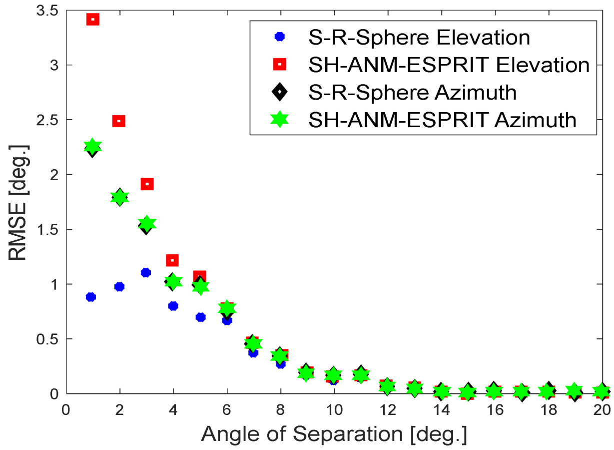

Figure 2. Error in DOA estimation against angle of separation in an ideal (no noise) single snapshot scenario.

6.2. Behavior under Uncorrelated Sources

The SHANM based approach is compared with the baselines using uncorrelated sources. It is assumed two equal power independent sources arrive at the SAA from $(\theta, \varphi) = (30^\circ, 60^\circ)$ and $(40^\circ, 130^\circ)$. A total of 250 snapshots were employed per trial and SNR values varied from 0 to 20 dB.

The RMSE values of the SH-ANM-ESPRIT, TSDA, SH-ESPRIT, and CV-VSBL approaches are as depicted in Figure 3. For azimuth, SH-ANM-ESPRIT gives a similar level of accuracy as the TSDA approach, and gives better performance in elevation estimation. In addition, the proposed method exhibits superiority in performance when compared with other methods. It is important to note that the $l_1 - norm$ dependent approach shows worse performance among sparsity-based approaches. This could be because of the problem faced while choosing the regularization variable, and the impacts to the truncating SVD processing.

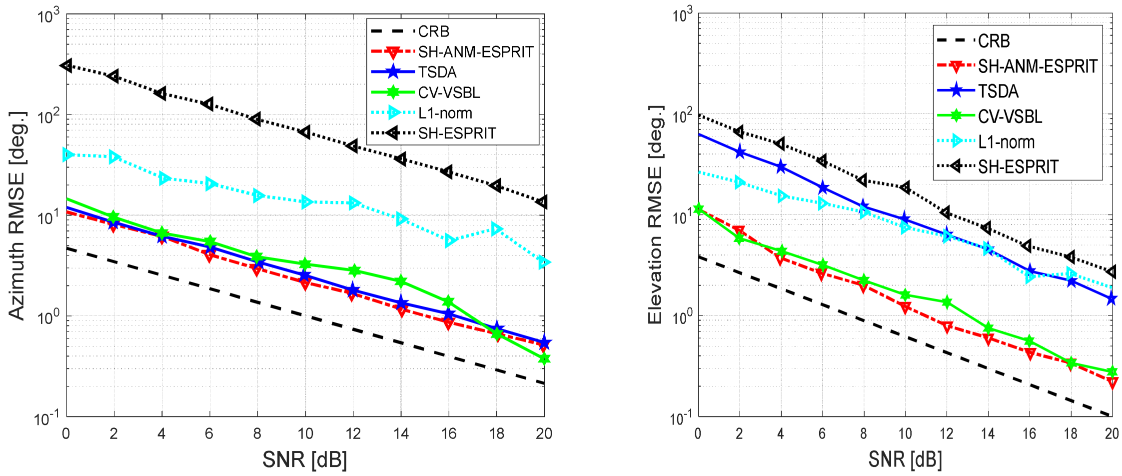

(**a**) (**b**)

Figure 3. Comparison of performance at various SNRs under uncorrelated sources at $(\theta, \varphi) = (30^\circ, 60^\circ)$ and $(40^\circ, 130^\circ)$. SNR is from 0 dB to 20 dB, 250 snapshots. (**a**) Azimuth. (**b**) Elevation.

Furthermore, a comparison of the methods against the number of snapshots at 0 dB SNR is presented. Two uncorrelated sources are positioned at $(\theta, \varphi) = (30^\circ, 60^\circ)$ and $(36^\circ, 138^\circ)$. Figure 4 shows that SH-ANM-ESPRIT exhibits the best performance.

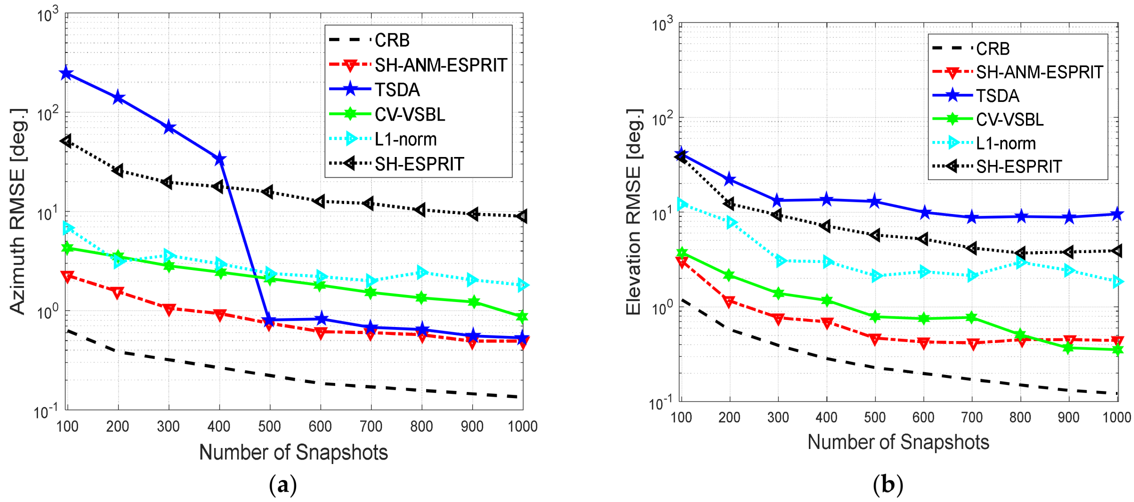

Figure 4. Comparison of performance with different value of snapshots under uncorrelated sources at $(\theta, \varphi) = (30^\circ, 60^\circ)$ and $(36^\circ, 138^\circ)$, 0 dB SNR. (**a**) Azimuth. (**b**) Elevation.

In addition, the SH-ANM-ESPRIT method is compared with the $l_1 - norm$, CV-VSBL, TSDA, and SH-ESPRIT methods against the angle of separation in terms of resolution probability. The interval of the grid is between 1° with 3 dB SNR. Assuming two uncorrelated sources are at $(\theta, \varphi) = (30^\circ, 60^\circ)$ and $(40^\circ + \vartheta, 60^\circ + \vartheta)$, the elevation of two signals requiring solution and that both $|\hat{\theta_1} - \theta_1|$ and $|\hat{\theta_2} - \theta_2| < |\theta_1 - \theta_2|/2$, and the probability of resolution of the azimuth could be described in a similar way.

In all, the SH-ANM-ESPRIT approach performs better than other approaches, as demonstrated in Figure 5. Therefore, SH-ANM-ESPRIT shows a super-resolution ability of DoA estimation.

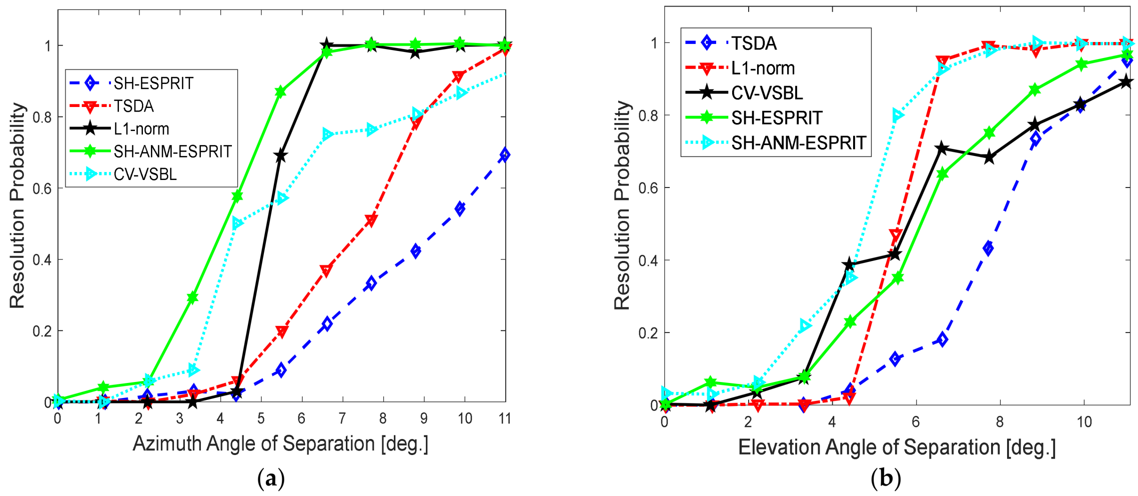

Figure 5. Resolution probability against angle of separation under uncorrelated sources at $(\theta, \varphi) = (40^\circ, 60^\circ)$ and $(40^\circ + \vartheta, 60^\circ + \vartheta)$, 3 dB SNR. (**a**) Azimuth. (**b**) Elevation.

6.3. Behavior under Correlated Sources

This subsection investigates, under correlated sources, the level of robustness of all methods. The two sources are in the same position with the results given in Figure 3 using the wave correlation coefficient $\alpha = 0.7$ and 250 snapshots. Figure 6 shows the illustration of the RMSE of all the approaches against the SNR. It can be observed that using correlated sources, each subspace-dependent approaches degrades in performance when compared with the uncorrelated sources scenario; however, the SH-ANM-ESPRIT approach is robust with regard to correlated signals. Estimating the azimuth, the SH-ANM-ESPRIT approach achieves the best accuracy level among all approaches, as the SNR varies from 10 dB to 20 dB. The performance of the SH-ANM-ESPRIT approach is satisfactory for elevation estimation.

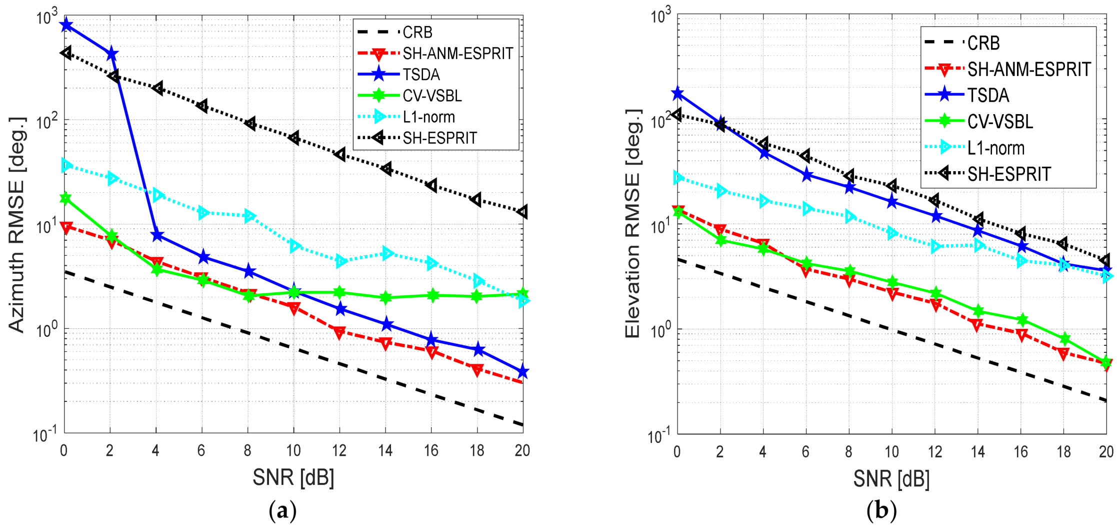

Figure 6. Comparison of performance with various SNRs under correlated sources $(\theta, \varphi) = (30^\circ, 60^\circ)$ and $(40^\circ, 130^\circ)$, 250 snapshots, and $\alpha = 0.7$. (**a**) Azimuth. (**b**) Elevation.

Figure 7 shows the RMSE performance of the proposed method, SH-ESPRIT, TSDA, and $l_1 - norm$ against snapshots, where it is assumed two correlated sources situated at $(\theta, \varphi) = (30^\circ, 60^\circ)$ and $(36^\circ, 138^\circ)$ with $\alpha = 0.8$ and 5 dB SNR. The results shows SH-ANM-ESPRIT gives a high level of robustness in relation to highly correlated sources.

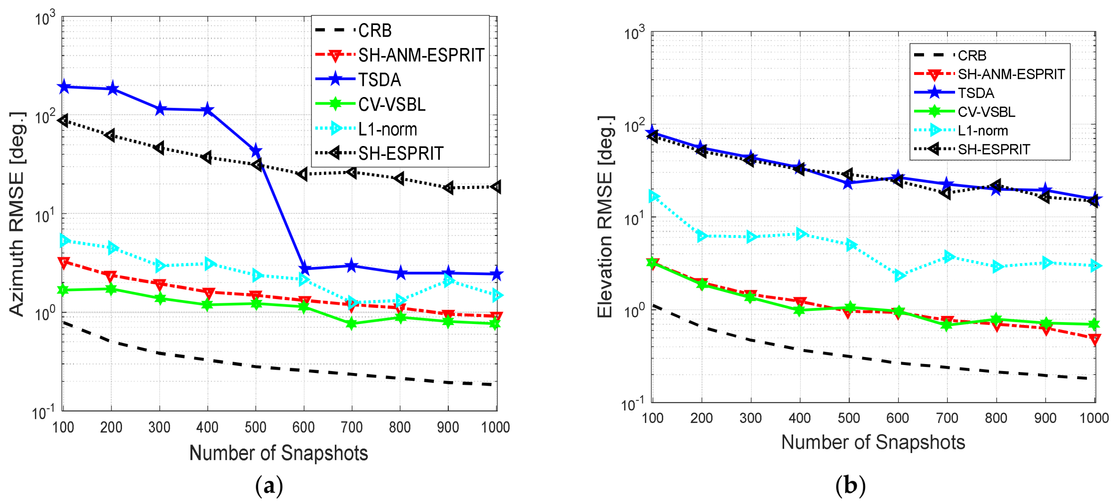

Figure 7. Comparison of performance with different value of snapshots under correlated sources at $(\theta, \varphi) = (30^\circ, 60^\circ)$ and $(36^\circ, 138^\circ)$, $\alpha = 0.8$. (**a**) Azimuth. (**b**) Elevation.

6.4. Experimental Measured Data

In order to fulfil the developing requirement and applications, a particular element's number is located on the systems. The inter-element spacing has become smaller, which leads to serious mutual coupling, causing poor radiation performance, and impedance matching [1,5,11]. Incorporating the impact of the mutual coupling problem in between the radiators, a practical measurement data, which is the most acceptable basis for testing any method, is employed. Hence, experimental data are also employed to analyze and evaluate the performance of the proposed method against the baselines. The antenna array is situated at the center of an anechoic chamber. The source is located at 74 DoAs, and received from the various merging of four elevations and eighteen various azimuths. The azimuths from 5° to 365° with 20 degree step size were selected. Comprehensive detail regarding the measurement setup is as presented in Figure 8 [8], where the measured data were originally published. Performance comparison between SH-ANM-ESPRIT, TSDA, SH-ESPRIT, and CV-VSBL were conducted. The gross error (GE) of the estimated DoA for each method against the SNR is processed and the results are as shown Figure 9. The SH-ANM-ESPRIT shows superiority in performance among all the methods, even with mutual coupling effect.

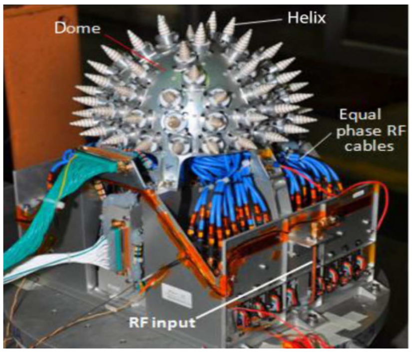

(**a**)

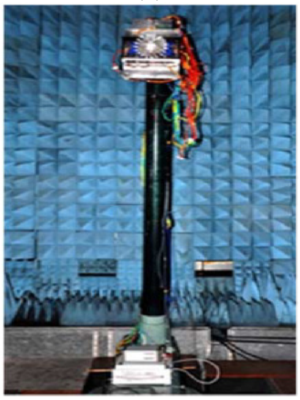

(**b**)

Figure 8. Experimental setup for measurement using an SAA. (**a**) SAA. (**b**) Configuration of the SPAA in anechoic chamber [8].

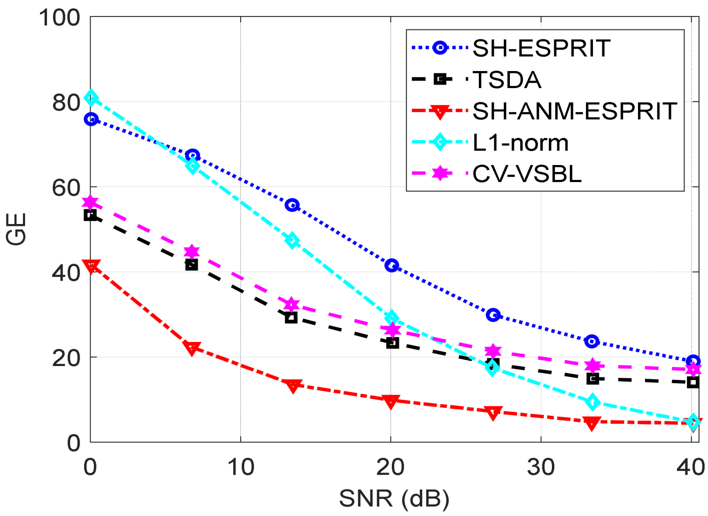

Figure 9. GE versus SNR performance using real measured data for various approaches.

7. Conclusions

In conclusion, this paper presents a SHANM-based DoA estimation method for EM waves impinging on an SAA configuration. A gridless sparse electromagnetic wave recovery is considered in the spherical harmonic domain in conjunction with the ANM. Because of the unavailability of the Vandermonde structure for the SH, the theorem of Vandermonde decomposition that is the mathematical basis of the traditional ANM methods find no application in the SH. Addressing this challenge, a low-dimensional SDP approach implementing the SHANM method is developed. This approach is independent of the decomposition of Vandermonde, and directly recovers the atomic decomposition in the SH. The simulation results show the superiority of the proposed method against the state of the art. Furthermore, considering the mutual coupling impacts, experimental measured data, which in the end, is the ground truth to test any procedure, is employed to illustrate the efficiency and robustness of the proposed SHANM-based DoA estimation method. Finally, both simulation and experimental results are inspiring enough towards practical deployment of the SHANM-based method for DoA estimation with enough accuracy of localization using an SAA.

Author Contributions: Conceptualization, O.J.F.; methodology, O.J.F. and T.S.; software, T.S.; validation, O.J.F. and T.S.; formal analysis, O.J.F.; resources, T.S.; writing—original draft preparation, O.J.F.; writing—review and editing, O.J.F. and T.S.; supervision, T.S. All authors have read and agreed to the published version of the manuscript.

Funding: The APC was funded by University of Johannesburg.

Institutional Review Board Statement: Not applicable.

Informed Consent Statement: Not applicable.

Data Availability Statement: Not applicable.

Conflicts of Interest: The authors declare no conflict of interest.

References

1. Famoriji, O.J.; Shongwe, T. Multi-source DoA estimation of EM waves impinging spherical antenna array with unknown mutual coupling using relative signal pressure based multiple signal classification approach. *IEEE Access* **2022**, *12*, 103793–103803. [CrossRef]
2. Fahim, A.; Samarasinghe, P.N.; Abhayapala, T.D. PSD estimation and source separation in a noisy reverberant environment using a spherical microphone array. *IEEE/ACM Trans. Audio Speech Lang. Process.* **2018**, *26*, 1594–1607. [CrossRef]
3. Asano, F.; Goto, M.; Itou, K.; Asoh, H. Real-time sound source localization and separation system and its application to automatic speech recognition. In Proceedings of the 7th European Conference on Speech Communication and Technology, Aalborg, Denmark, 3–7 September 2001; pp. 1013–1016.
4. Adavanne, S.; Politis, A.; Nikunen, J.; Virtanen, T. Sound event localization and detection of overlapping sources using convolutional recurrent neural networks. *IEEE J. Sel. Top. Signal Process.* **2019**, *13*, 34–48. [CrossRef]
5. Famoriji, O.J.; Shongwe, T. Subspace Pseudointensity Vectors Approach for DoA Estimation Using Spherical Antenna Array in the Presence of Unknown Mutual Coupling. *Appl. Sci.* **2022**, *12*, 10099. [CrossRef]
6. Kumar, P.; Kumar, C.; Kumar, S.; Srinivasan, V. Active spherical phased array design for satellite payload data transmission. *IEEE Trans. Antennas Propagat.* **2015**, *63*, 4783–4791. [CrossRef]
7. Knott, P. Design and experimental results of a spherical antenna array for a conformal array demonstrate. In Proceedings of the 2007 2nd International ITG Conference on Antennas, Munich, Germany, 28–30 March 2007; pp. 1–4.
8. Famoriji, O.J.; Ogundepo, O.Y.; Qi, X. An intelligent deep learning-based direction-of-arrival estimation scheme using spherical antenna array with unknown mutual coupling. *IEEE Access* **2020**, *8*, 179259–179271. [CrossRef]
9. Hu, Y.; Abhayapala, T.D.; Samarasinghe, P.N. Multiple source direction of arrival estimations using relative sound pressure based MUSIC. *IEEE/ACM Trans. Audio Speech Lang. Process.* **2020**, *29*, 253–264. [CrossRef]
10. Carlin, M.; Rocca, P.; Oliveri, G.; Viani, F.; Massa, A. Directions-of-arrival estimation through Bayesian compressive sensing strategies. *IEEE Trans. Antennas Propagat.* **2013**, *61*, 3828–3838. [CrossRef]
11. Famoriji, O.J.; Shongwe, T. Source localization of EM waves in the near-field of spherical antenna array in the presence of unknown mutual coupling. *Wirel. Commun. Mob. Comput.* **2021**, *2021*, 3237219. [CrossRef]
12. Tervo, S.; Politis, A. Direction of arrival estimation of reflections from room impulse responses using a spherical microphone array. *IEEE/ACM Trans. Audio Speech Lang. Process.* **2015**, *23*, 1539–1551. [CrossRef]

13. Famoriji, O.J.; Shongwe, T. Critical review of basic methods on DoA estimation of EM waves impinging a spherical antenna array. *Electronics* **2022**, *11*, 208. [CrossRef]
14. Evers, C.; Löllmann, H.W.; Mellmann, H.; Schmidt, A.; Barfuss, H.; Naylor, P.A.; Kellermann, W. The LOCATA challenge: Acoustic source localization and tracking. *IEEE/ACM Trans. Audio Speech Lang. Process.* **2020**, *28*, 1620–1643. [CrossRef]
15. Famoriji, O.J.; Shongwe, T. Direction-of-arrival estimation of electromagnetic wave impinging on spherical antenna array in the presence of mutual coupling using a multiple signal classification method. *Electronics* **2021**, *10*, 2651. [CrossRef]
16. Rafaely, B. Plane-wave decomposition of the pressure on a sphere by spherical convolution. *J. Acoust. Soc. Am.* **2004**, *116*, 2149–2157. [CrossRef]
17. Teutsch, H.; Kellermann, W. EB-ESPRIT: 2D localization of multiple wideband acoustic sources using Eigen-beams. In Proceedings of the IEEE International Conference on Acoustics, Speech, and Signal Processing, Philadelphia, PA, USA, 18–23 March 2005; Volume 3, pp. iii/89–iii/92.
18. Khaykin, D.; Rafaely, B. Coherent signals direction-of-arrival estimation using a spherical microphone array: Frequency smoothing approach. In *IEEE Workshop on Applications of Signal Processing to Audio and Acoustics*; IEEE: New Paltz, NY, USA, 2009; pp. 221–224.
19. Jarrett, D.P.; Habets, E.A.P.; Naylor, P.A. 3D source localization in the spherical harmonic domain using a pseudointensity vector. In Proceedings of the 18th European Signal Processing Conference, Aalborg, Denmark, 23–27 August 2010; pp. 442–446.
20. Rafaely, B.; Peled, Y.; Agmon, M.; Khaykin, D.; Fisher, E. Spherical microphone array beamforming. In *Speech Processing in Modern Communication: Challenges and Perspectives*; Cohen, I., Benesty, J., Gannot, S., Eds.; Springer: New York, NY, USA, 2010; pp. 281–305.
21. Sun, H.; Mabande, E.; Kowalczyk, K.; Kellermann, W. Localization of distinct reflections in rooms using spherical microphone array Eigenbeam processing. *J. Acoust. Soc. Am.* **2012**, *131*, 2828–2840. [CrossRef]
22. Evers, C.; Moore, A.H.; Naylor, P.A. Multiple source localization in the spherical harmonic domain. In Proceedings of the 14th International Workshop on Acoustic Signal Enhancement (IWAENC), Nice, France, 8–11 September 2014; pp. 258–262.
23. Nadiri, O.; Rafaely, B. Localization of multiple speakers under high reverberation using a spherical microphone array and the direct-path dominance test. *IEEE/ACM Trans. Audio Speech Lang. Process.* **2014**, *22*, 1494–1505. [CrossRef]
24. Moore, A.H.; Evers, C.; Naylor, P.A.; Alon, D.L.; Rafaely, B. Direction of arrival estimation using pseudointensity vectors with direct path dominance test. In Proceedings of the 23rd European Signal Processing Conference (EUSIPCO), Nice, France, 31 August–4 September 2015; pp. 2296–2300.
25. Roshani, S.; Shahveisi, H. Mutual coupling reduction in microstrip patch antenna arrays using simple microstrip resonator. *Wirel. Pers. Commun.* **2022**, *126*, 1665–1677. [CrossRef]
26. Liao, B. Fast angle estimation for MIMO radar with nonorthogonal waveforms. *IEEE Trans. Aerosp. Electron. Syst.* **2018**, *54*, 2091–2096. [CrossRef]
27. Wang, H.; Wan, L.; Dong, M.; Ota, K.; Wang, X. Assistant vehicle localization based on three collaborative base stations via SBL based robust DOA estimation. *IEEE Internet Things J.* **2019**, *6*, 5766–5777. [CrossRef]
28. Rauhut, H.; Ward, R. Sparse recovery for spherical harmonic expansions. *arXiv* **2011**, arXiv:1102.4097. Available online: https://arxiv.org/abs/1102.4097 (accessed on 5 December 2022).
29. Burq, N.; Dyatlov, S.; Ward, R.; Zworski, M. Weighted eigen function estimates with applications to compressed sensing. *SIAM J. Math. Anal.* **2012**, *44*, 3481–3501. [CrossRef]
30. Huang, Q.; Zhang, G.; Fang, Y. Real-valued DOA estimation for spherical arrays using sparse Bayesian learning. *Signal Process.* **2016**, *125*, 79–86. [CrossRef]
31. Dai, W.; Chen, H. Multiple speech sources localization in room reverberant environment using spherical harmonic sparse Bayesian learning. *IEEE Sens. Lett.* **2019**, *3*, 7000304. [CrossRef]
32. Huang, Q.; Kai, L.; Xiang, L. Off-grid DOA estimation in real spherical harmonics domain using sparse Bayesian inference. *Signal Process.* **2017**, *137*, 124–134. [CrossRef]
33. Chandrasekaran, V.; Recht, B.; Parrilo, P.A.; Willsky, A.S. The convex geometry of linear inverse problems. *Found. Comput. Math.* **2012**, *12*, 805–849. [CrossRef]
34. Candès, E.J.; Fernandez-Granda, C. Towards a mathematical theory of super-resolution. *Commun. Pure Appl. Math.* **2014**, *67*, 906–956. [CrossRef]
35. Chi, Y.; Chen, Y. Compressive two-dimensional harmonic retrieval via atomic norm minimization. *IEEE Trans. Signal Process.* **2015**, *63*, 1030–1042. [CrossRef]
36. Yang, Z.; Xie, L.; Stoica, P. Vandermonde decomposition of multilevel toeplitz matrices with application to multidimensional superresolution. *IEEE Trans. Inf. Theory* **2016**, *62*, 3685–3701. [CrossRef]
37. Xu, W.; Cai, J.-F.; Mishra, K.V.; Cho, M.; Kruger, A. Precise semidefinite programming formulation of atomic norm minimization for recovering D-dimensional (D-2) off-the-grid frequencies. In Proceedings of the Information Theory and Applications Workshop (ITA), San Diago, CA, USA, 9–14 February 2014; pp. 1–4.
38. Mishra, K.V.; Cho, M.; Kruger, A.; Xu, W. Spectral super-resolution with prior knowledge. *IEEE Trans. Signal Process.* **2015**, *63*, 5342–5357. [CrossRef]
39. Li, Y.; Chi, Y. Off-the-grid line spectrum denoising and estimation with multiple measurement vectors. *IEEE Trans. Signal Process.* **2016**, *64*, 1257–1269. [CrossRef]

40. Yang, Z.; Xie, L.; Zhang, C. A discretization-free sparse and parametric approach for linear array signal processing. *IEEE Trans. Signal Process.* **2014**, *62*, 4959–4973. [CrossRef]
41. Wu, X.; Zhu, W.-P.; Yan, J. A Toeplitz covariance matrix reconstruction approach for direction-of-arrival estimation. *IEEE Trans. Veh. Technol.* **2017**, *66*, 8223–8237. [CrossRef]
42. Steffens, C.; Pesavento, M.; Pfetsch, M.E. A compact formulation for the $\ell_{2,1}$ mixed-norm minimization problem. *IEEE Trans. Signal Process.* **2018**, *66*, 1483–1497. [CrossRef]
43. Bendory, T.; Dekel, S.; Feuer, A. Exact recovery of Dirac ensembles from the projection onto spaces of spherical harmonics. *Constr. Approx.* **2015**, *24*, 183–207. [CrossRef]
44. Roemer, F.; Semper, S.; Hotz, T.; Galdo, G.D. Grid-free direction-of-arrival estimation with compressed sensing and arbitrary antenna arrays. In Proceedings of the IEEE International Conference on Acoustics, Speech and Signal Processing (ICASSP), Calgary, AB, Canada, 15–20 April 2018; pp. 3251–3255.
45. Mahata, K.; Hyder, M.M. Grid-less T.V minimization for DOA estimation. *Signal Process.* **2017**, *132*, 155–164. [CrossRef]
46. Mahata, K.; Hyder, M.M. Fast frequency estimation with prior information. *IEEE Trans. Signal Process.* **2018**, *66*, 264–273. [CrossRef]
47. Bendory, T.; Dekel, S.; Feuer, A. Super-resolution on the sphere using convex optimization. *IEEE Trans. Signal Process.* **2015**, *63*, 2253–2262. [CrossRef]
48. Pan, J. Spherical Harmonic Atomic Norm and Its Application to DOA Estimation. *IEEE Access* **2019**, *7*, 156555–156568. [CrossRef]
49. Famoriji, O.J.; Shongwe, T. Electromagnetic machine learning for estimation and mitigation of mutual coupling in strongly coupled arrays. *ICT Express* **2023**, *9*, 8–15. [CrossRef]
50. Rafaely, B. Analysis and design of spherical microphone arrays. *IEEE Trans. Speech Audio Process.* **2015**, *13*, 135–143. [CrossRef]
51. Lebedev, V.I.; Skorokhodov, A.L. Quadrature formulas of orders 41, 47 and 53 for the sphere. *Russ. Acad. Sci. Dokl. Math.* **1992**, *45*, 587–592.
52. Yin, J.; Chen, T. Direction-of-arrival estimation using a sparse representation of array covariance vectors. *IEEE Trans. Signal Process.* **2011**, *59*, 4489–4493. [CrossRef]
53. Tang, G.; Bhaskar, B.N.; Shah, P.; Recht, B. Compressed sensing off the grid. *IEEE Trans. Inf. Theory* **2013**, *59*, 7465–7490. [CrossRef]
54. Panahi, A.; Viberg, M. Performance analysis of sparsity-based parameter estimation. *IEEE Trans. Signal Process.* **2017**, *65*, 6478–6488. [CrossRef]
55. Goossens, R.; Rogier, R. Closed-form 2D angle estimation with a spherical array via spherical phase mode excitation and esprit. In Proceedings of the IEEE International Conference on Acoustics, Speech and Signal Processing (ICASSP), Las Vegas, Nevada, 31 March–4 April 2008; pp. 2321–2324.
56. Wu, P.K.T.; Epain, N.; Jin, C. A dereverberation algorithm for spherical microphone arrays using compressed sensing techniques. In Proceedings of the IEEE International Conference on Acoustics, Speech and Signal Processing (ICASSP), Kyoto, Japan, 25–30 March 2012; pp. 4053–4056.
57. Huang, Q.; Fang, Y.; Zhang, L. Two-stage decoupled DOA estimation based on real spherical harmonics for spherical arrays. *IEEE/ACM Trans. Audio Speech Lang. Process.* **2017**, *25*, 2045–2058. [CrossRef]
58. Kumar, L.; Hegde, R.M. Stochastic Cramér-Rao bound analysis for DOA estimation in spherical harmonics domain. *IEEE Signal Process. Lett.* **2015**, *22*, 1030–1034. [CrossRef]